Solar RRL

WILEY VCH

Solar RRL

RESEARCH ARTICLE OPEN ACCESS

Monitoring Charge Separation of Individual Cells in Perovskite/Silicon Tandems via Transient Surface Photovoltage Spectroscopy

Maxim Simmonds[1] | Ke Xu[1] | Steve Albrecht[1,2] | Lars Korte[1,2] | Igal Levine[3]

[1]Solar Energy Division, Helmholtz-Zentrum Berlin für Materialien und Energie GmbH, Berlin, Germany | [2]Faculty of Electrical Engineering and Computer Science, Technical University Berlin, Berlin, Germany | [3]Institute of Chemistry and The Center for Nanoscience and Nanotechnology, The Hebrew University of Jerusalem, Jerusalem, Israel

Correspondence: Lars Korte (korte@helmholtz-berlin.de) | Igal Levine (igal.levine@mail.huji.ac.il)

Received: 28 April 2025 | **Revised:** 12 June 2025 | **Accepted:** 17 June 2025

Funding: Federal Ministry of Education and Research, Grant/Award Number: 03EE1123C; German State of Lower Saxony; German-Israeli Helmholtz International Research School HI-SCORE, Grant/Award Number: HIRS-0008

Keywords: buried interface | charge extraction | heterojunction solar cell | perovskite/silicon tandem | surface photovoltage

ABSTRACT

Identification of charge carrier separation processes in perovskite/silicon tandem solar cells and recombination at buried interfaces of charge selective contacts are crucial for photovoltaic research. Here, intensity- and wavelength-dependent transient surface photovoltage (tr-SPV) is used to investigate slot-die-coated perovskite top layers deposited on n-type heterojunction silicon bottom cells. We show that using an appropriate combination of photon energy and/or bottom cell polarity, one can individually probe the buried interfaces of the bottom silicon cell or the perovskite's buried interfaces of a tandem solar cell: for excitation with higher energy photons, time delays before the onset of a strong SPV signal indicate significant hole minority drift before separation in the silicon bottom cells. Furthermore, symmetric bottom Si heterojunction solar cell stacks can serve to investigate the top perovskite stack including its junction to the bottom cell, unhampered by photovoltages from the silicon substrate. Thus, investigation of the buried interfaces in tandem devices using time-resolved surface photovoltage is found to yield valuable information on charge carrier extraction at buried interfaces and demonstrates its unique potential compared to more conventional approaches that rely on photoluminescence decay kinetics.

1 | Introduction

Perovskite/silicon (Si) tandem solar cells have demonstrated high solar energy conversion efficiencies in the past few years. Most of the highest-efficiency solar cells are now based on n-type silicon, marking a significant shift from the previous dominance of p-type wafers in 2024 [1–3]. Nowadays, the most efficient solar cells are silicon heterojunction (SHJ) cells using crystalline silicon (c-Si) wafers as the absorber and hydrogenated amorphous or nanocrystalline silicon/silicon oxides (a-Si:H or nc-Si:H/nc-SiOx:H) to form the contacts for charge extraction. Such SHJ cells are also used in today's most efficient perovskite/silicon tandem cells [4], which make them strong candidates for upscaling and industrialization [5].

A full tandem solar cell stack is comprised of many different layers that result in numerous interfaces. Optoelectronic characterization of the individual electronic junctions that are formed in each of these interfaces is a challenging task, not only because most of them are buried interfaces, but also because they can be affected by the overall built-in field within the device. Using Kelvin probe and photoelectron yield spectroscopy to measure

SPV, we recently demonstrated the importance of the built-in field (or: voltage) in the perovskite cell device stack for charge carrier separation and its crucial dependence on the contact metal's work function [6]. To date, most optoelectronic characterization of tandem solar cells is done by absolute or transient photoluminescence (tr-PL) [7–9] and current (density)–voltage (J–V) measurements both in the dark and under illumination. These methods enable investigation of various properties but suffer several drawbacks. To name a few, J–V characterization requires fabrication of the entire device including electrical contacts, which does not allow investigation of a single interface. Using tr-PL, one cannot disentangle interfacial defect-assisted recombination from charge extraction (e.g., blocked transport by energetic misalignment at the interfaces) without additional measurements [10]. Thus, understanding fill factor losses and quantifying the charge carrier dynamics at a specific interface over various time regimes of full tandem solar cells remains a longstanding challenge.

This work is dedicated to analyzing the charge carrier dynamics occurring in slot-die-coated perovskite thin film coated on two different bottom Si heterojunction structures: (1) a heterojunction solar cell on n-type c-Si, and (2) a c-Si (n)/ nc-SiOx:H (n+) symmetric Si heterojunction, by utilizing excitation wavelength and intensity-dependent, transient surface photovoltage (transient SPV or tr-SPV) measurements. In contrast to J–V and PL measurements, SPV measurements do not require electrical contacts and do not suffer from the ambiguity that tr-PL presents when disentangling carrier extraction from nonradiative recombination. This allows to investigate and isolate individual interfaces even in very complicated layer stacks, by studying the layers in a step-wise manner. Furthermore, since tr-SPV relies on electrical detection of the change in the surface potential, rather than photons as in the case of tr-PL, a significant gain in sensitivity can be obtained, which is especially beneficial when studying materials with extremely low photoluminescence quantum yield. An SPV signal is generated upon light-induced separation of charge carriers, with the direction of charge separation given by the sign of the SPV signal [11]. A positive (negative) SPV signal indicates the separation of holes (electrons) being displaced toward the SPV probe's surface. Our previous study on single-junction perovskite solar cells demonstrated that tr-SPV measurements yield valuable information on the charge carrier dynamics in buried interfaces over a wide time range from nanoseconds to seconds [10]. Varying the excitation wavelength allows exciting separately the Si bottom cell or the perovskite top cell, provided that the top cell absorbs close to all photons excited. Such selective excitation of the bottom and top cells individually was recently applied using electrochemical impedance spectroscopy by Roose et al.[12], demonstrating how the response of the individual cells can be recorded separately, yet it still requires an often-complex electrical circuit modeling, which can be omitted by using tr-SPV.

In the following, a low repetition rate of 2 Hz is employed to fully capture the charge carrier dynamics after photoexcitation and observe minute differences in the tr-SPV decays that could originate from very slow recombination processes, slow diffusion of carriers within the bulk of the c-Si, trapping/de-trapping of charge carriers from deep traps, and back-injection of charge carriers into the absorber layers.

First, we show an energy band diagram for the Si bottom cells to present similarities and differences in the different stacks used. Next, wavelength-dependent and intensity-dependent tr-SPV are recorded and investigated for the different layer stacks. Last, based on the differences in the tr-SPV transients between the samples, a model that describes the charge separation and recombination processes is introduced and discussed.

2 | Results and Discussion: Tandem Stacks and Band Alignment

The two types of tandem architectures are shown in Figure 1A, B for the SHJ and symmetric-SHJ, respectively. In both cases, the light absorber of the top cells is an 800 nm thick triple-halide perovskite layer ($Cs_{0.22}FA_{0.78}Pb$ $(I_{0.85}Br_{0.15})_3$ + 5 mol% $MAPbCl_3$ (hereafter named perovskite) with 1.68 eV bandgap. As a hole extraction contact to the perovskite layer (hole transport layer, hereafter named HTL), a self-assembled monolayer of 2PACz ([2-(9H-Carbazol-9-yl)ethyl]phosphonic acid) was deposited on the ITO substrate. The key difference between the SHJ and symmetric-SHJ stems from the presence or absence of the p+/n selective junction (hole contact) at the back of the tandem stack. The nc-SiOx:H (n) is a surface field layer that minimizes surface recombination and improves the ohmic contact to the ITO layer. Analogously to the HTL in perovskite solar cells as hole selective layer, the nc-SiOx (n) acts as charge selective layer (for electrons, in this case), but provides almost no built-in field. The n+/n/n+ stack in Figure 1B is thus an 'all-electron' majority carrier device. Electrons can easily flow through it toward the tunnel-recombination junction with the perovskite top cell, but due to its symmetry and negligible band bending at both interfaces, no (pronounced) net SPV signal can build up in the n+/n/n+ stack. The lack of band bending is exemplified in Figure S3 (comparison of p+/n/n+ versus n+/n/n+), where the SPV amplitude is greatly reduced for the symmetric-SHJ solar cell.

Hence, by employing a symmetric back contact, we effectively suppress bottom-cell-related contributions, allowing for an unambiguous investigation of the buried perovskite front interface.

Next, we focus our attention on tr-SPV measurements for both the SHJ and the symmetric-SHJ bottom cells, covered with thick triple-halide perovskite layers.

2.1 | Wavelength-Dependent SPV

To study the charge carrier dynamics in the individual subcells of the tandem structure, wavelength-dependent tr-SPV measurements were performed, as shown in Figure 2. By selecting the laser excitation wavelength, we selectively excite either only the bottom cell, or mainly the top perovskite cell. To obtain a good signal-to-noise ratio across all photon energies, relatively high laser fluences were used. However, we ensured that the photon flux is nearly constant at different wavelengths, as shown in Figure S2 in the Supplementary information. All observed SPV values were negative as expected: since both subcells have holes

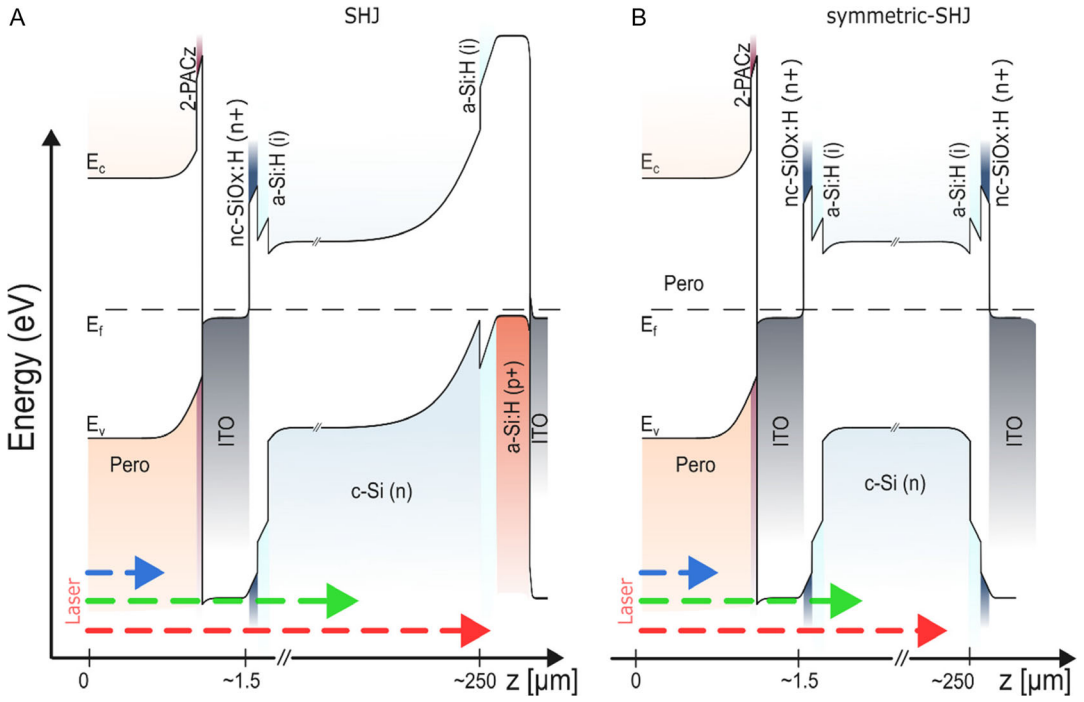

FIGURE 1 | Sketch of the estimated energy band diagrams (neglecting interface dipole for the 2-PACz layer), including the illumination direction; (A) SHJ: n-type Floatzone (FZ) Si (c-Si (n)) heterojunction with an a-Si:H (p+) layer on the rear side of the Si bottom cell (SHJ) and a triple-halide perovskite top cell. (B) Symmetric-SHJ: n-type FZ Si (c-Si (n)) heterojunction cell with nc-SiOx:H (n+) layers on both sides of the Si wafer and a slot-die-coated triple-halide perovskite top cell. In both cases, the Si wafer was ~250 µm thick.

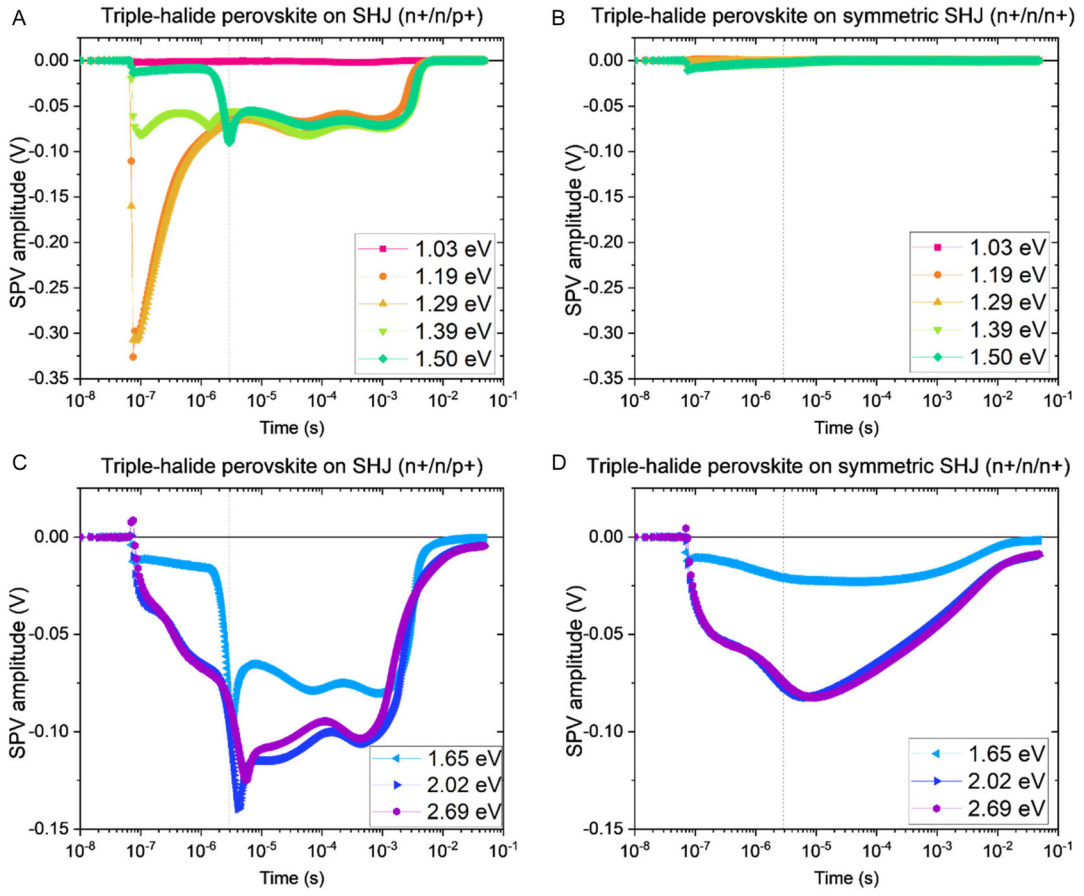

FIGURE 2 | Transient-SPV signals for SHJ (A, C) and symmetric SHJ (B, D) using front (perovskite side) illumination at different excitation wavelengths (1.03–2.69 eV) and a repetition rate of 2 Hz. The silicon substrate is approximately 250 µm thick.

extracted toward their respective rear contact (right side Figure 1A,B), while electrons are separated toward the front side where the SPV electrode is located.

Starting with the tandem with an SHJ bottom cell in Figure 2A, excitation from 1.03 to 1.50 eV is purely absorbed by the Si absorber (for the external quantum efficiency (EQE) spectra of both subcells, see Figure S6 in the Supplementary information). At 1.19 eV, the inverse of the absorption coefficient is $\alpha^{-1} \approx 1000\,\mu m$ for Si [13], meaning the generation profile in the silicon wafer is homogeneous. For this case, we observe a sharp and fast initial SPV peak of 326 mV. A higher photon energy of 1.50 eV (where $\alpha^{-1} \approx 19\,\mu m$, with carriers generated toward the front contact Si junction), results initially in a small negative SPV of around 12 mV, which remains nearly constant for around 3 µs. We explain this small first initial SPV as corresponding to the reduction of the weaker front contact band bending in the Silicon absorber. This leads to extraction of electrons into the front recombination ITO layer. Afterward, a sharp, delayed second rise in the SPV is observed. The SPV signal remains rather constant up to 3 µs. This suggests that the number of photogenerated electrons and holes, which were separated in space, did not increase during this period. This is because in the SHJ, the electron–hole pairs photo-generated at the Si front side undergo ambipolar diffusion into the Si bulk with different electron and hole mobilities until they reach the rear side selective layer (hole contact), reducing the stronger back contact band bending and leading to hole extraction, generating a second delayed and stronger rise in SPV. Under similar photon fluence, the SPV with 1.19 eV excitation attains a peak value of −326 mV whereas the 1.39 eV excitation yields only −70 mV after 2 µs. This can be explained due to recombination of electron–hole pairs during the diffusion of these carriers to the rear n/p+ interface. Note that the recombination of electron–hole pairs during diffusion will correspond to decreased performance of a solar cell. Hence, assuming our interpretation of the results is correct, the tr-SPV measured on the perovskite/SHJ stack at a photon energy of 2.69 eV indicates that the back contact band bending is suppressed due to the arrival and extraction of holes 6 µs after the excitation pulse (SPV maximum in Figure 2C, purple curve). To quantitatively confirm this interpretation, diffusion simulations were conducted (Supplementary Notes SI.6 and SI.7). The differential equations ES1 and ES2 account for carrier diffusion as well as nonradiative Shockley–Read–Hall (defect recombination) and Auger processes. Note that these simulations are drift-only and do not account for possible transient effects due to electric fields caused by the dynamics of charge redistribution. To compensate for this limitation, we use known ambipolar diffusion coefficients, which incorporate the coupling of electrons and holes via their Coulombic attraction.

At a photon energy of 1.5 eV, the simulations show that the ambipolar arrival time is approximately $\tau_{ambipolar} = 17\,\mu s$ (see Figure S7C), indicating that carriers require on average 17 µs to diffuse through the full 250 µm wafer thickness. This value is about three times larger than the experimentally observed SPV peak time, $\tau_{exp} = 6\,\mu s$ (see Figure 2A, green curve).

At 6 µs after the laser pulse, we estimate that carriers have diffused an average distance of $L_{exp} = \sqrt{2D_{ambipolar}\tau_{exp}} = 130\,\mu m$, as derived from Fick's law, using $D_{ambipolar} = 14.3\,cm^2\,s^{-1}$ (from ref. [14]). This implies that only carriers photogenerated within the final 130 µm from the back can contribute to canceling the back contact band bending, at $t < \tau_{exp}$.

To test this hypothesis, we evaluate whether there are enough photogenerated carriers present within this region. For this, we integrate the carrier density over the final 130 µm of the wafer and assume these carriers reside within the back contact band bending region. This gives:

$$\Delta p_{\text{back}} = \frac{\int_{L-L_d}^{L} \Delta p(x)dx}{L_{\text{inversion}}} = 2.210^{16}\,cm^{-3} \quad (1)$$

with $L_{inversion} \approx 500\,nm$ [15], corresponding to the thickness of the back contact band bending region. This excess carrier concentration corresponds to a quasi-Fermi level splitting (QFLS) of:

$$QFLS = kT \ln\left(\frac{\Delta p_{\text{back}}^2}{n_i^2}\right) \approx 750\,meV \quad (2)$$

which agrees well with the expected value for the built-in potential of an SHJ (~800 meV) [16].

Therefore, the initially photogenerated carriers within the rear 130 µm of the wafer are sufficient to suppress a significant portion of the back contact band bending. This supports our interpretation that early SPV signals ($\tau_{exp} < \tau_{ambipolar}$) originate from these carriers generated in the bulk of the wafer reaching and neutralizing the back contact field, before the full diffusion of carriers.

Ambipolar diffusion of charge carriers can also explain the shifts in the observed times of the second SPV peaks of Figure 2A. As the excitation wavelength decreases, photogeneration takes place further away from the rear side, resulting in larger diffusion lengths and hence longer diffusion times (see the two green curves of Figure 2A, as well as Figure S3A). To further prove that the ambipolar diffusion plateau is related to the Si bottom cell only, an independent measurement was conducted on a 250 µm Floatzone Heterojunction Si substrate (without a perovskite layer, shown in Figure S3 A and B), where similar charge carrier dynamics were observed. The diffusion simulation results of Figure S7 also show that the resulting electron arrival times indeed increase as a function of photon energy and will saturate for photon energies larger than 1.5 eV. The saturation value at E > 1.5 eV in Figure S7C is consistent with the saturation of the SPV peak time. Thus, based on **a)** the experimental confirmation that an SHJ-only cell exhibits an SPV plateau at early times (see Figure S3A), along with **b)** simulation results that align with the experimentally observed increase in carrier arrival time as a function of photon energy, and **c)** the observed decrease in arrival time with increasing pulse power (Figure 3, with further discussion in the next section), we conclude that the delayed SPV rise is indeed caused by ambipolar diffusion of photogenerated electrons and holes toward the rear side of the silicon wafer.

Interestingly, although ambipolar diffusion has been observed and investigated in silicon previously, it has been rarely discussed in the context of SHJ solar cells. This is primarily because earlier studies typically illuminated SHJ devices from the p/n-junction

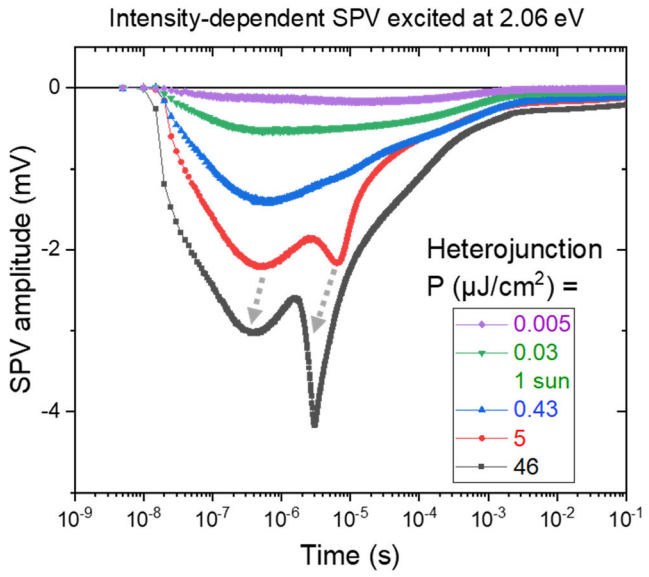

FIGURE 3 | Intensity-dependent transient SPV measurements for perovskite on a silicon heterojunction cell with front side illumination at 600 nm laser excitation at 2 Hz repetition rate.

side to evaluate interface quality and carrier extraction efficiency [17]. Under such conditions, the ambipolar diffusion signal is largely masked by the dominant response associated with the cancelation of band bending in the p/n junction.

In contrast, the front-side illumination used in Si/perovskite tandem devices on n-type wafers—where light enters from the top while the p/n junction resides at the back of the Si cell—brings ambipolar diffusion effects to the forefront. Our results thus identify ambipolar diffusion as a significant charge transport mechanism in SHJ silicon cells with a rear p-contact under tandem-relevant conditions.

That said, we do not expect this ambipolar signal to introduce significant performance losses in tandem applications. Indeed, the most efficient single-junction silicon solar cells today also employ heterojunction p-contacts on the wafer's rear side, interdigitated with n-the n-type contact—namely, the heterojunction back-contact (HBC) design [18, 19]. Furthermore, in tandem configurations, only low-energy photons reach the silicon bottom cell. Thus, the photogeneration profile in the Si wafer is less depth-dependent in tandems than in a Si single junction solar cell. As such, ambipolar transport in these devices is unlikely to limit overall performance.

For the SHJ tandem, in the 1.6–2.7 eV range (Figure 2C), as the excitation wavelength decreases, more and more electron–hole pairs are generated in the perovskite layer. Therefore, the initial peak at 0.37 μs (which is absent from the Si-only SHJ cell as shown in Figure S3 A and B, as expected) is related to hole extraction to the HTL underneath the perovskite layer. The holes extracted from the perovskite layer then recombine at the interface to the n-type ITO layer, which supplies the electrons required as recombination partners. Note that in the measurement conditions presented, we still observe the delayed SPV peak (at 1 μs) linked to the extraction of holes at the n/p+ interface on the rear of the silicon bottom cell.

To further separate the different contributions of the perovskite/HTL hole extraction interface and the silicon n/p+ interface, tr-SPV was also measured for symmetric-SHJ stacks as substrates for the perovskite top cell. Replacing the (n/p+) junction at the Si wafer's rear with an n/n+ contact suppresses the signal from the bottom silicon cell while keeping the exact same processing steps and overall structure for the perovskite top cell. This assures device-relevant properties of the perovskite cell stack. The results are plotted in Figure 2B,D. First, at lower energies (Figure 2B), we confirm that the SPV signal emerging from the silicon bottom cell was effectively suppressed. Similarly to the early rise for the SHJ (Figure 2A), we do observe slight negative signals for 1.4 and 1.5 eV excitations. Again, we ascribe this to the elimination of the weaker front n/n+ band bending, accompanied by injection of electrons from the n-silicon into the n+ contact. It is of interest that for the longer wavelengths, no such signal is observed. There the small front and rear opposing built-in fields are both suppressed, leading to SPV signals that cancel out, which we ascribe to be due to a more homogeneous generation profile.

Finally, in Figure 2D, at higher excitation energies (Si + Pero excitation), we show the presence of a negative SPV signal. In comparison to Figure 2B, we do not observe any delayed SPV rise at 1 μs. Therefore, the observed signal mainly originates from the top perovskite solar cell, with much reduced contribution from the bottom silicon cell. We also confirm this by showing that the tr-SPV signal of a perovskite/HTL sample deposited on ITO glass (Figure S4) is comparable to the 'isolated top cell' signal of Figure 2D. There, we observe a reduction of the plateau at early times for the glass/ITO/HTL/perovskite as compared to the symmetric SHJ/ITO/HTL/perovskite sample. We relate this loss of SPV to the possible re-injection of extracted holes into the perovskite layer when there are no extra free electrons available in the ITO deposited on glass. In contrast, the recombination ITO of the tandem stack should contain extra free electrons from the excited back silicon cell, inducing electron (silicon extracted) hole (perovskite extracted) recombination and resulting in a more sustained SPV. However, other mechanisms are also possible to explain the differences of Figure S4 and exact identification is out of the scope of this work.

To conclude, we demonstrate that with wavelength-dependent SPV measurements, one can isolate the contributions of the perovskite front and silicon bottom cells in such tandem architectures. Additionally, we show that the use of a substrate with symmetric contacts – in our case, an n+/n/n+ SHJ - effectively suppresses the signal of bottom silicon solar cells while preserving the processing sequence as well as SHJ top contact serving as the perovskite substrate, and thus the properties of the perovskite top cell. tr-SPV on such a symmetric substrate thus results in the probing of a highly isolated and device-relevant perovskite top cell, paving way for effective optimization of the top perovskite cell stack as well as process parameters.

2.2 | Intensity-Dependent SPV

To better understand the interplay between the charge carrier generation in both absorbers, and its effect on the band bending, in Figure 3, the intensity was varied at a constant 600 nm

(2.06 eV) excitation wavelength to excite both absorbers simultaneously (according to the EQE plots shown in Figure S6, 87.5% absorption by the perovskite, and 3.0% by the silicon). The equivalent photogenerated carrier concentrations range from 5×10^{18} cm^{-3} for 46 μJ cm^{-2} to 5×10^{14} for 0.005 μJ cm^{-2}. We note that the equivalent laser fluence for 1-sun illumination is 0.03 μJ cm^{-2} (green curve), corresponding to 3×10^{15} cm^{-3}. From 0.005 to 0.43 μJ cm^{-2}, the SPV recombination dynamics were similar to that of a single-junction perovskite cell [10], suggesting that nearly all photogeneration occurs within the perovskite layer.

The transients shown in Figure 3 exhibit a combination of charge extraction processes from the perovskite absorber and a shifted delayed SPV peak originating from the Si bottom cell. At an intensity of 0.43 μJ cm^{-2}, the major contribution to the SPV signal comes from the perovskite layer, as can be seen from the peak time of 0.59 μs in agreement with the extraction times observed for single-junction perovskite-only half cells utilizing 2PACz as an HTL [10]. At higher intensities, from 5 to 46 μJ cm^{-2}, we observe the appearance of an ambipolar diffusion peak. The peak onset decreases from 7.8 to 3.7 μs. This reduction in peak onset time is explained by inspecting the electron and hole arrival times at the back of the Silicon wafer. Using our diffusion model (note S8 in the Supplementary information), we observe that a reduction of charge arrival time is expected as the incoming photon flux increases, as shown in Figure S8, corroborating the experimental observations of Figure 3. Also, we show that the reduction of arrival time is solely due to the diffusion term of ES1 and ES2 (see Figure S9): therefore, the reduction of peak SPV time is a signature of the ambipolar diffusion of carriers within the c-Si wafer.

3 | Charge Separation Model Deduced from SPV Transients over a Wide Time Range

Finally, Figure 4 illustrates the processes that we have considered in our transients. The case of low energy photons ($E_{phot} < 1.3$ eV) is not depicted here, as it does not contain any valuable information on the perovskite cell: The perovskite is transparent at this photon energy, and photogenerated charges are close to homogeneously distributed in the Si absorber. This leads to an immediate reduction of band bending at the rear p+/n contact, thus a sharp increase in SPV, followed by a monotonous decrease in the signal. This behavior is fully governed by the c-Si bottom cell's properties. Next, we consider a photon energy of 1.5 eV (Figure 4, upper panel). Here, the perovskite is still transparent, whereas the absorption depth, α^{-1}, in c-Si is ca. 40 μm. The initial negative SPV signal at ~ 20 ns originates from photogenerated charge carriers that undergo separation close to the recombination ITO layer. Because the a-Si:H (p) layer is located 250 μm away at the rear, ambipolar diffusion of the remaining electron–hole pairs to the rear side occurs on the timescale of ~2–4 μs. When the electron–hole pairs reach the rear side selective layer (hole contact), the electron–hole pairs are immediately separated at the rear junction, giving rise to the second, delayed negative SPV signal at ~2 μs. The following slow decay corresponds to the recombination within the Si bottom cell and/or due to the ambipolar diffusion of carriers (where slower photogenerated holes redistribute after electrons, effectively 'catching up' electrons). For the 2.7 eV excitation (Figure 4, bottom purple curve), a small positive signal is observed at around 10 ns, which could be explained by electron trapping at the ITO/HTL interface [10]. In the regime between 30 ns–1 μs, the signal is composed of charge separation by the perovskite/HTL interface and by the separation of electrons photogenerated in the Si toward the recombination ITO. During the first few μs, ambipolar diffusion occurs within the c-Si layer, again giving rise to the second delayed negative SPV peak at ca. 3–6 μs, followed by delayed charge separation by the rear side in the junction with the a-Si (p). The slow decay after 6 μs corresponds to back transfer and recombination of the remaining charge carriers in the different layers.

Due to the complexity of the cell architectures studied here, we refrain from establishing a direct correlation between the tr-SPV

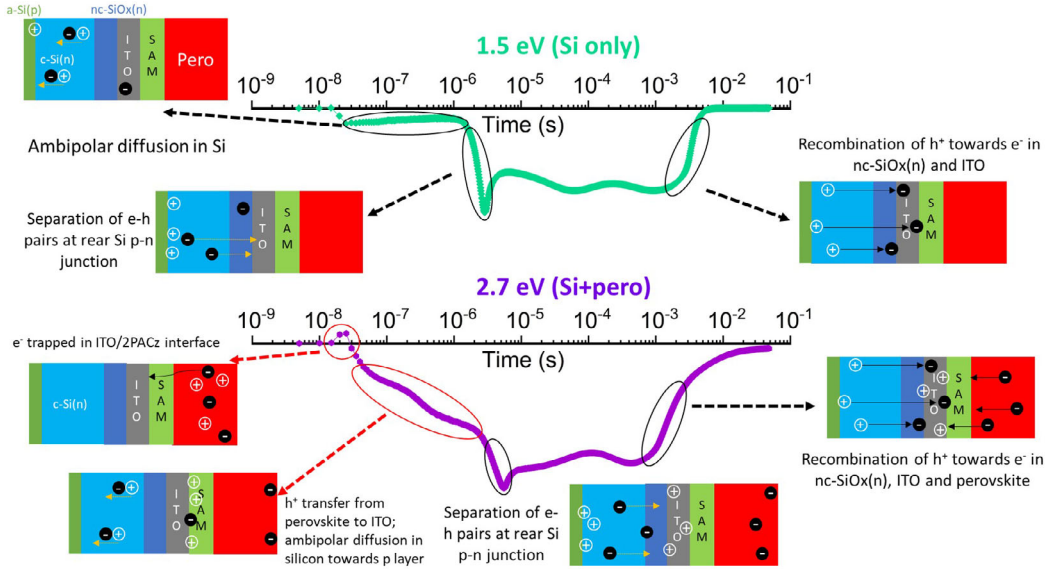

FIGURE 4 | Summary of the different suggested phenomena explaining the SPV transients over a wide time range for a perovskite / n-type heterojunction tandem layer stack for 1.5 eV (Si-only excitation, green curve, top), and 2.7 eV excitation (Si+pero excitation, purple curve, bottom). For clarity, charge separation processes related to the perovskite layer only are highlighted in red.

kinetics and the actual tandem solar cell PV parameters (shown in Figure S5). Still, one would expect that larger tr-SPV amplitudes that are maintained over a relatively large time window would directly translate to a larger Voc, while faster SPV rise times for each subcell will translate to larger FF. However, future studies that include drift-diffusion simulations will be focused on addressing the influence of the individual layers on the tr-SPV kinetics and solar cell parameters simultaneously, establishing the correlation between tr-SPV decays of tandem layer stacks and device performance.

4 | Conclusion

In this work, perovskite films with a bandgap of 1.68 eV slot-die coated on heterojunction and symmetric heterojunction Si bottom cells were investigated by wavelength-dependent time-resolved surface photovoltage measurements. The results showed delayed charge separation for lower energy photons in the silicon bottom cell. Ambipolar diffusion of electron–hole pairs to the rear p–n junction of the heterojunction Si bottom cell was found to be the cause of a delayed SPV signal. At high photon energies, a symmetric SHJ tandem showed an isolated signal from the top perovskite cell whereas the SHJ tandem showed a convolved signal from the bottom and top cells. Two main conclusions are drawn toward the results. First, with photon energies lower than the bandgap of the perovskite top cell, we isolate the bottom silicon cell. While selective excitation was used for this purpose previously in transient photocurrent measurements [20], tr-SPV does not require a top contact and hence allows to study partial cell stacks, thus investigating the influence of individual interfaces. Second, using a symmetric SHJ bottom silicon cell, we demonstrate an isolated SPV signal originating from the top perovskite cell. Thus, an in-depth analysis of the charge carrier dynamics of a tandem-equivalent perovskite cell stack is demonstrated, using spectrally resolved tr-SPV with the combination of symmetric and nonsymmetric bottom c-Si cells.

With the ability to effectively isolate single interfaces from the bottom or top cell, the methodology shown here can be applied to gain valuable insights into the carrier dynamics of different perovskite silicon tandem architectures and pin-point losses at interfaces to select appropriate charge transport layers for the perovskite top cell, in-route for tandems approaching their theoretical limit.

Acknowledgments

The authors thank Thomas Dittrich for fruitful discussions and for providing SPV lab facilities for the tr-SPV measurements, and Isaac Balberg and Hannes Hempel for fruitful discussions. The authors acknowledge the Helmholtz Association for funding within the HySPRINT Innovation lab and the Zeitenwende project as well as the Federal Ministry of Education and Research (BMWK) for funding the projects SHAPE (grant no. 03EE1123C), as well as funding from the German State of Lower Saxony in project "NextGenPV" through funding program "zukunft.niedersachsen". M.S. is grateful for support by the German–Israeli Helmholtz International Research School HI-SCORE (HIRS-0008).

Conflicts of Interest

The authors declare no conflicts of interest.

Data Availability Statement

The data that support the findings of this study are available from the corresponding author upon reasonable request.

References

1. C. Messmer, B. S. Goraya, S. Nold, et al., "The Race for the Best Silicon Bottom Cell: Efficiency and Cost Evaluation of Perovskite-Silicon Tandem Solar Cells," *Progress in Photovoltaics: Research and Applications* 29 (2021): 744–759.

2. H. Lin, M. Yang, X. Ru, et al., "Silicon Heterojunction Solar Cells with up to 26.81% Efficiency Achieved by Electrically Optimized Nanocrystalline-Silicon Hole Contact Layers," *Nature Energy* 8 (2023): 789–799.

3. VDMA (2024). International Technology Roadmap for Photovoltaic (ITRPV) - 2023 Results.

4. LONGi "*34.85%! LONGi Breaks World Record for Crystalline Silicon-Perovskite Tandem Solar Cell Efficiency Again*," (2025): https://www.longi.com/en/news/silicon-perovskite-tandem-solar-cells-new-world-efficiency/.

5. E. Aydin, T. G. Allen, M. De Bastiani, et al., "Pathways toward Commercial Perovskite/Silicon Tandem Photovoltaics," *Science* 383 (2024): eadh3849.

6. E. Gutierrez-Partida, M. Rusu, F. Zu, et al., "Toward Understanding the Built-in Field in Perovskite Solar Cells through Layer-by-Layer Surface Photovoltage Measurements," *ACS Applied Materials and Interfaces* 17 (2025): 11176–11186.

7. M. Stolterfoht, M. Grischek, P. Caprioglio, et al., "How To Quantify the Efficiency Potential of Neat Perovskite Films: Perovskite Semiconductors with an Implied Efficiency Exceeding 28%," *Advanced Materials* 32 (2020): 2000080.

8. F. Lang, E. Köhnen, J. Warby, et al., "Revealing Fundamental Efficiency Limits of Monolithic Perovskite/Silicon Tandem Photovoltaics through Subcell Characterization," *ACS Energy Letters* 6 (2021): 3982–3991.

9. J. Warby, F. Zu, S. Zeiske, et al., "Understanding Performance Limiting Interfacial Recombination in Pin Perovskite Solar Cells," *Advanced Energy Materials* 12 (2022): 2103567.

10. I. Levine, A. Al-Ashouri, A. Musiienko, et al., "Charge Transfer Rates and Electron Trapping at Buried Interfaces of Perovskite Solar Cells," *Joule* 5 (2021): 2915–2933.

11. S. F. Thomas Dittrich, Surface Photovoltage Analysis of Photoactive Materials (World Scientific, 2020).

12. B. Roose, K. Dey, M. R. Fitzsimmons, et al., "Electrochemical Impedance Spectroscopy of All-Perovskite Tandem Solar Cells," *ACS Energy Letters* 9 (2024): 442–453.

13. M. A. Green, "Self-Consistent Optical Parameters of Intrinsic Silicon at 300 K including Temperature Coefficients," *Solar Energy Materials and Solar Cells* 92 (2008): 1305–1310.

14. PV lighthouse. "*PV light house PV Light House: Mobility Calculator*," https://www2.pvlighthouse.com.au/calculators/Mobility%20calculator/Mobility%20calculator.aspx.

15. R. Varache, "*Development, Characterization and Modeling of Interfaces for High Efficiency Silicon Heterojunction Solar Cells*," (Technische Universität Berlin, Fakultät IV - Elektrotechnik und Informatik, 2013), https://doi.org/10.14279/depositonce-3599.

16. R. Varache, J. P. Kleider, M. E. Gueunier-Farret, et al., "Silicon Heterojunction Solar Cells: Optimization of Emitter and Contact Properties from Analytical Calculation and Numerical Simulation," *Materials Science and Engineering B: Solid-State Materials for Advanced Technology* 178 (2013): 593–598.

17. L. Korte, A. Laades, K. Lauer, et al., "Surface Photovoltage Investigation of Recombination at the a-Si/c-Si Heterojunction," *Thin Solid Films* 517 (2009): 6396–6400.

18. LONGi, *LONGi Sets New World Record with 27.30% for Heterojunction Back Contact Cells and Renames Next Generation Silicon Tera Wafer to TaiRay Wafer* (2024), https://www.longi.com/eu/news/2730-hbc-world-record/.

19. M. A. Green, E. D. Dunlop, M. Yoshita, et al., "Solar Cell Efficiency Tables (Version 66)," *Progress in Photovoltaics: Research and Applications* 33 (2025): 795–810.

20. A. Ghorai, P. Kumar, S. Mahesh, et al., "Insights into the Charge Carrier Dynamics in Perovskite/Si Tandem Solar Cells Using Transient Photocurrent Spectroscopy," *Applied Physics Letters* 120 (2022): 173504.

Supporting Information

Additional supporting information can be found online in the Supporting Information section.